Progress In Electromagnetics Research, Vol. 154, 127–141, 2015

Simulating Wave Phenomena in Large Graded-Pattern Arrays with Random Perturbation

Davood Ansari Oghol Beig[1], Jierong Cheng[1], Cristian D. Giovampaola[2], Amirnader Askarpour[3], Andrea Alu[3], Nader Engheta[2], and Hossein Mosallaei[1, *]

Abstract—Efficient and accurate computer simulation of wave phenomena plays an important role in invention, development, cost reduction and optimization of many systems ranging from ultra-high-speed electronics to delicate nanoscale optical devices and systems. Understanding the physics of many modern technological applications such as optical nanomaterials calls for the solution of very complex computer models involving hundreds of millions to billions of unknowns. Integral equation (IE) methods are increasingly becoming the method of choice when comes to numerical modeling of wave phenomena for various reasons specifically since the introduction of FMM and MLFMA acceleration that tremendously reduce the computational costs associate with naive implementation of IE methods. In this work, a new acceleration technique specifically designed for the modeling of large, inhomogeneous, finite array problems it introduced. Specifically we use the new method for modelling and design of some metamaterial structures. At last, the presented method is used to study the some of the undesired random effects that occur in metamaterial array fabrication.

1. INTRODUCTION

Wave phenomena and array structures are indispensable parts of today's developments. The interest in the study of waves in finite and infinite (pseudo-)array structures traditionally stemmed from crystal physics and x-ray crystallography. Nonetheless, the advent of modern technologies such as optical metamaterials (MMs), micro- and nano-electro-mechanical systems and acoustic MMs has boosted the interest in efficient simulation methods for wave phenomena. Furthermore, many other applications, such as the study of waves in complex and random media can also be formulated as wave phenomena in randomly perturbed (pseudo-)array structures.

Unlike dissipative and local phenomena, waves are known for their ability to demonstrate long distance interactions and to carry information encoded in their phase (latency) characteristics. Computer modeling of continuum problems involves the discretization of geometrical models and governing equations using various numerical techniques. Such numerical techniques are in general classified into two major categories, differential-equation-(DE) and integral-equation-(IE) based methods. In finite-difference time-domain (FDTD) methods, the time domain representation of the governing partial differential equations is converted into a set of difference equations expressed over an equally spaced grid [1, 2]. Other methods, such as the finite-element method (FEM), assign polynomial representations [3] to the unknown physical quantity on an unstructured grid, such as a nonuniform triangular/tetrahedral mesh and apply variational methods to find the optimal polynomial coefficients that minimize the resulting residual in the governing equations [4]. Both FEM and FDTD are based upon satisfaction of the governing equations in their DE form, and hence they are both regarded as DE

Received 4 October 2015, Accepted 17 December 2015, Scheduled 29 December 2015

* Corresponding author: Hossein Mosallaei (hosseinm@ece.neu.edu).

[1] Department of Electrical Engineering, Northeastern University, USA. [2] Department of Electrical and Systems Engineering, University of Pennsylvania, USA. [3] Department of Electrical and Computer Engineering, University of Texas, Austin, USA.

based methods. On the other hand, IE based methods rely on the representation of the unknown physical quantity in terms of unknown representative sources. Such representations are obtained by means of the Green's theorem and involve integral operators acting on the representative sources. Quite importantly here, one must recognize that for wave phenomena the propagation delay is encoded in the Green's function (GF) of the problem [5, 6] in exact form. When it comes to computer modeling of waves, all DE-based numerical simulation methods (FEM, FD) suffer from inaccuracies in modeling propagation latency when numerically emulated waves travel in the model over increasingly long distances. This is due to the fact that emulated waves exhibits different propagation characteristics, e.g., speed, depending on the size and shape of the discretization used in the computer model, as well as on the propagation direction of the wave. Due to this effect, also known as numerical dispersion [2, 7], waves in the computer model tend to propagate faster or slower than they should. The situation becomes more pronounced when structured grids are used, e.g., in the FDTD method with a uniform rectangular grid, since the rectangular elements in the model are all of the same size and have the same orientation, resulting in a coherent accumulation of error in the propagation delay. When the mathematical description of a wave problem is Fourier-transformed into its equivalent frequency domain representation, the propagation latency is transformed into a harmonic phase and thus it is customary to speak about the phase error instead of the propagation latency error. Proper retrieval of phase information is key to the correct modeling of wave phenomena for large domains [8] and this is one of the most prominent reasons that IE-based techniques are favored over DE-based methods in computer modeling of light-matter interaction. Many of the fundamental properties of waves, as opposed to local or diffusive phenomena like heat, can be discerned by analyzing the behavior of the so-called free-space GF associated with the governing partial differential equations. The GF for a scalar phenomenon in an isotropic medium is usually of the form $\frac{e^{-\jmath kr}}{r}$, where for waves $\Re k > 0$ (this is also regarded as hyperbolic PDE with an oscillatory kernel), and where for other local or diffusive phenomena one encounters $\Re k \leq 0$ [8].

In essence, an IE-based method solves a linear system of equations where the system matrix inherits many of its properties directly from the underlying GF of the problem. In a naive implementation, computations with such a system of equations results in a computational complexity of $\mathcal{O}(N)^2$ just for the construction and storage of the system of equations, where N is the number of discretization elements. This is so, since one has to consider all possible interactions between all N discrete components of the computer model. Nonetheless, modern computational techniques such as the fast multipole method (FMM) [9–11], multilevel fast multipole method (MLFMM) [12], and FFT-based accelerators [13, 14] have significantly reduced the computational costs to nearly linear functions of the number of system unknowns N.

In this work, we present the application of a recently introduced method regarded as 'Array Integral Equation Fast Fourier Transform' (A-IE-FFT) method [28], to some representative examples that highlight the importance of the technique in the above-mentioned modeling applications. Moreover, we will provide proof-of-concept simulation examples demonstrating its feasibility and highlighting its remarkable computational efficiency in problems involving large arrays. A main advantage of this approach is that in many problems it yields $\mathcal{O}(1)$ storage complexity for all near interactions, the importace of which may be appreciated from the example problems presented in this work.

2. MATHEMATICAL FORMULATION

The numerical examples of presented in this work are based on IE solution of Maxwell's equations. For this purpose, an integral equation representation of the problem must be adopted. Since these examples involve wave scattering in penetrable media, a JMCFIE formulation is adopted for this purpose [28, 29]. The formulation is briefly stated here for the sake of consistency. Using equivalence principle and field representation formula, The following two equations each specify the total field balance on a closed surface Γ separating two subdomain Ω_1 and Ω_2:

$$\mathcal{A}_1 : \begin{bmatrix} -\eta_1 \mathscr{L}_1^- & \mathscr{K}_1^- \\ -\mathscr{K}_1^- & -\frac{1}{\eta_1}\mathscr{L}_1^- \end{bmatrix} \begin{bmatrix} +\mathcal{J} \\ +\mathcal{M} \end{bmatrix} = - \begin{bmatrix} \mathcal{E}_1^{inc} \\ \mathcal{H}_1^{inc} \end{bmatrix} \tag{1}$$

$$\mathcal{A}_2 : \begin{bmatrix} -\eta_2 \mathscr{L}_2^- & \mathscr{K}_2^- \\ -\mathscr{K}_2^- & -\frac{1}{\eta_2}\mathscr{L}_2^- \end{bmatrix} \begin{bmatrix} -\mathcal{J} \\ -\mathcal{M} \end{bmatrix} = - \begin{bmatrix} \mathcal{E}_2^{inc} \\ \mathcal{H}_2^{inc} \end{bmatrix} \tag{2}$$

In these equations, $\mathscr{L}_i^-$ and $\mathscr{K}_i^-$ are the limit of the electric and magnetic field operators as the observation points approach, from outside of Ω_i, the surface Γ enclosing Ω_i and where $\eta_i \triangleq \mu_i/\epsilon_i$ is the impedance of the homogeneous medium Ω_i. Here Ω_i is a homogeneous and simply connected subdomain of the problem. Also, $\mathcal{E}_i^{inc}$ and $\mathcal{H}_i^{inc}$ are the electrical and magnetic components of the incident fields. The electric field integral operator $\mathscr{L}^{\pm}$ is defined as

$$(\mathscr{L}_i^{\pm}\jmath)(\vec{r}_o) = \lim_{h\to 0}\left(-\jmath k\int_{\partial\Omega_i}\jmath(\vec{r}_s)g(|\vec{R}_h^{\pm}|)dS_o + \jmath\frac{1}{k}\nabla_o\int_{\partial\Omega_i}\jmath(\vec{r}_s)\cdot\nabla_s g(|R_h^{\pm}|)dS_s\right), \tag{3}$$

where $\vec{R}_h^{\pm} \triangleq \vec{r}_o - \vec{r}_s \pm h\hat{n}_i(\vec{r}_o)$ is the vector connecting a source point at $\vec{r}_s$ to an observation point at $\vec{r}_o$ (in the limit of $h\to 0$), where $g(R) \triangleq e^{-\jmath k|\vec{R}|}/(4\pi|\vec{R}|)$ is the homogeneous media GF with a wavenumber k, and where $\hat{n}_i$ is the surface normal on $\partial\Omega_i$ pointing into Ω_i at $\vec{r_o}$. Similarly the magnetic field integral operator $\mathscr{K}^{\pm}$ is defined as

$$(\mathscr{K}_i^{\pm}\jmath)(\vec{r}_o) = \lim_{h\to 0}\left(\int_{\partial\Omega_i}\nabla_s g(|\vec{R}_h^{\pm}|)\times\jmath(\vec{r}_s)dS_s\right). \tag{4}$$

With these definitions in place, the JMCFIE formulation is obtained from adding up the two Equations (1) and (2) with two coefficient matrices as

$$\begin{bmatrix} 1 & \eta_1\hat{n}_1\times \\ \hat{n}_1\times & +\eta_1 \end{bmatrix}\mathcal{A}_1 + \begin{bmatrix} 1 & \eta_2\hat{n}_2\times \\ \hat{n}_2\times & +\eta_2 \end{bmatrix}\mathcal{A}_2. \tag{5}$$

Since this the focus of this article is more on the new applications of the array-IE-FFT (A-IE-FFT) method, we refrain from diving too deep into the method itself and refer the interested reader to [28]. However, with (5) at hand, similar to other IE solvers a surface discretization of the integral equation results in a matrix equation of the form $[\mathsf{Z}_{ij}][\mathsf{x}_j] = [\mathsf{y}_i]$. Therefore, the solution of problems involving complex geometries leads to the solution linear system with large number of unknowns. Using direct factorizations methods, the cost associated with solving this system will become prohibitively expensive, i.e., proportional to the cubic power of the number of unknowns. Hence, the solution has to be found by means of iterative (optimization) methods. Loosely speaking, in an iterative method, each iteration requires calculating the action of on a given guess solution. In essence, this is equivalent to observing the field due to every source on every observation basis. Thus, using iterative matrix solvers, the solution process boils down to calculating the action of $[\mathsf{Z}_{ij}]$ on a sequence of guess vectors, and hence, being able to efficiently calculate the action of $[\mathsf{Z}_{ij}]$ on a given guess vector will be critical. Using the A-IE-FFT [28] method, this is achieved extremely efficiently for an important class of array-like problems as it is evident from the examples presented in this work. A detailed discussion on the A-IE-FFT method will deviate the discussion from the main intent of this article, i.e., important application of the method in large array MM design. The following section, however, the cons and the pros of this method are briefly discussed. A detailed presentation on the A-IE-FFT method can be found in [28].

3. PROS AND CONS OF A-IE-FFT METHOD

The A-IE-FFT method is a hybrid surface integral equation method specifically designed for fast and efficient modeling of MM array problems. Naive implementation of the IE methods results in undesired computational complexity of $\mathcal{O}(N^2)$ and $\mathcal{O}(N^3)$. However, this problem has been resolved with the introduction of fast multiple method (FMM) [9–11] followed by multi-level versions of FMM that can deliver $\mathcal{O}(N\log(N))$ complexity. Other IE acceleration techniques based on FFT, low rank representation and hierarchical matrices [18, 19] were also developed in parallel to FMM. Obviously enough, each of these methods offer superior performance over the others when applied to the right type of problem. It is the job of the computer analyst to identify, develop and implement the most suitable tool or method for a given problems. In this spirit, successful application of a computational electromagnetic simulation tool to full-scale MM problems requires the observation of certain critical aspects associated with class of problems:

(i) Pronounced level of near field interactions as opposed to far field interactions.

(ii) Sub-wavelength size building blocks.

(iii) Deep sub-wavelength size features.

(iv) Geometry repetition and (pseudo-)array structure.

(v) Large aperiodic structures consisting of tens of thousands of MM cells or building blocks.

The A-IE-FFT method, is a hybrid accelerated surface IE method that uses a hybridization of the hierarchical matrix method with a novel FFT accelerator that is built around the above-mentioned aspects of MM problems. A key in A-IE-FFT's efficiency is the use of a 6-level *Toeplitz* matrix instead of the conventionally known 3-level *Toeplitz* matrix used in FFT based IE accelerators [14]. Here, the extra three levels in the construction of the *Toeplitz* matrix correspond to the dimensions of the array structure as depicted in Fig. 1. This modification, eliminates the need for the near-field correction encountered in conventional IE-FFT method [14]. Moreover, observing that MM building blocks are essentially designed to measure smaller than the wavelength, the near field matrices used to represent the coupling between neighbouring building blocks are subject to the low frequency condition that allows for their efficient compression using the hierarchical matrix method [19]. Finally, the building-block based construction of the problem allows for recycling of building block information. This last feature, is of course a common advantage of many domain decomposition techniques. Another important feature that is integrated into the A-IE-FFT solver is the use of the equivalent surface (ES) method to encapsulate the building block details (without loss of accuracy) into the minimal set of unknowns that can determine the array-wide interactions [16, 17] and often significantly reduces the cost of *Krylov* iterations.

As depicted in Fig. 1, in A-IE-FFT method first the object of interest is dissected into small pieces and each piece is wrapped in an ES, on which, it is possible to solve the scattered field from the sub-scatterer solely in terms of the incident field distribution on the ES. Hence, by eliminating the unknowns associated with scatterer parts encapsulated in ESs, the calculation of the action of $[\mathsf{Z}_{ij}]$ will be equivalent to coupling the field from every ES box into every ES box, which means that the computational cost of order $\mathcal{O}(N^2)$ the operation is of order, N being the number of sub-scatterers. Similar to other IE acceleration methods including FMM [10–14], the couplings then can be classified into two groups, near (in this case between immediate neighboring boxes) and far: Fig. 1(b) symbolically depicts how one near coupling is done from one cell to another immediately neighboring cell while Fig. 1(c) shows how far coupling are implemented from individual sub-scatterers (or cells) to the A-IE-FFT grid and then back the cells. Although the sub-scatterers may have totally different geometries, the ESs can be chosen such that they look identical from outside. This choice, with respect to solution of array problems, leads to very important advantages if we classify the interactions between system components at the ES-to-ES level:

- FFT has been traditionally used to reduce the cost associated with handling of matrices arising from IE methods. An issue with FFT-based acceleration of IE methods is the loss of accuracy for near interactions, which has to be compensated by some other correction method [13, 14]. The presented A-IE-FFT method utilizes a six-level Toeplitz matrix structure [15] to eliminate the need for this near correction.
- Quite often, a large array problem consists of a small set of building blocks. Therefore, a small number of matrix blocks specifying the interaction of an ES with various building blocks need to be calculated; Fig. 2, shows a model of random media consisting of randomly distributed spherical cavities inside a denser medium. A very large random array of such media can be realized from a finite number of building blocks and the random nature of the model can be preserved by a random placement of the building blocks in the array. Thus, the self matrix storage can often be constant with respect to array size. Fig. 2, presents a typical example for problems in which a random media can be realized as the result of randomly concatenating instances of a fixed set of building blocks. The importance of such problems, however, is better understood when we realize that such problems are encountered in various fields, ranging from the study of optical diffusers used in LCD backlighting to propagation of seismic wave in porous media.
- By means of a fictitious enclosing boundary or an ES, the coupling between each box and its immediate neighbors needs to be calculated and stored only for $26 = 3 \times 3 \times 3 - 1$ cases as it is independent of its enclosed sub-scatterer [16, 17]. This is in contrast with other methods such as

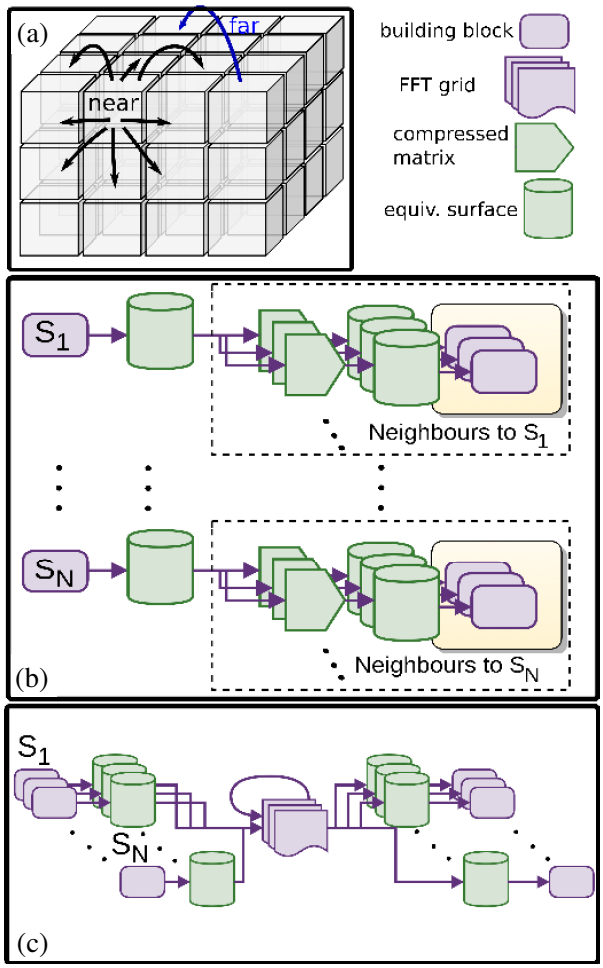

Figure 1. Block diagram representation of the A-IE-FFT method, (a) fictitious boxes signifying the subdivision of the problem in A-IE-FFT. The arrows are showing some of the ES-to-ES couplings that occur in the array. (b) Handling of near interactions in A-IE-FFT. The number of these is proportional to the number of boxes since every box has finite number of neighbors. (c) Handling of far interactions in A-IE-FFT. The number of coupling operations from building blocks to ES's (and vice-versa) is equal to the number of boxes.

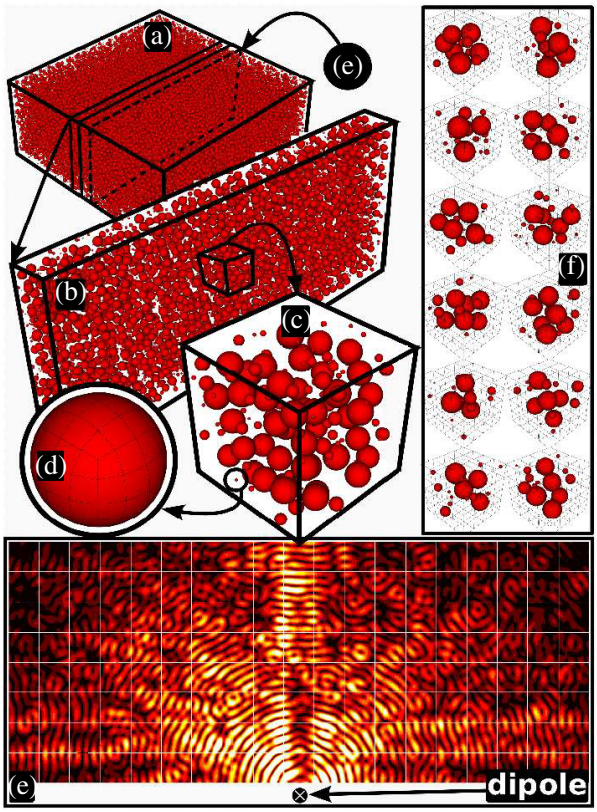

Figure 2. Random porous media with 114.8 million unknowns consisting of randomly sized and distributed air bubbles in a dense dielectric background medium with a dielectric constant of $\epsilon_r = 9$. The field is excited with an electric dipole perpendicular to the plane of the image. (a) The complete model. (b) A slice of (a). (c) A smaller portion of (b). (d) One of the spheres in the model depicting the higher-order curvilinear mesh. (e) Normalized real part of the tangential magnetic field plotted on a section of the media as depicted in (a). (f) The twelve random building blocks use for the construction of the complete model.

MLFMA where the near-field coupling storage grows linearly, i.e., with N being the number of MLFMA boxes [12].

- As depicted in Fig. 1, usually only the interactions between immediate neighbouring boxes must be treated as near interactions. This implies that, given that all ES boxes are the same, only 26 ($3 \times 3 \times 3 - 1$) types of neighboring box-to-box coupling matrices need to be computed. These matrices can be highly processed and compressed using methods such as the hierarchical matrix representation [18, 19] thus reducing the cost of their storage and application. The choice of

identically shaped ES comes as a natural consequence of the array-like nature of the problem. This is particularly straightforward when the problem is made from disjoint scatterers. However, this restriction can also be alleviated by means of (touching) domain decomposition techniques as well as the use of a dual coarse-fine discretization grid for the ESs.

4. RESULTS

4.1. Metamaterial Lens

The concept of digital MM is an analogue to the ideas behind *Boolean* algebra that lead to the invention and development of the digital computer, which despite the systematic complexity, operate on the incredibly simple concepts of *Boolean* algebra and digital logic. It is envisioned and shown that limiting the choices of materials used in the design and fabrication of MM systems, leads to an analogous simplicity that is key to the successful realization and fabrication of complex MM systems. Specifically, a proper mixture of only two elemental materials can lead to effective material parameters different from the original ones. Hence, we use the concept of digital MMs to the realization of an optical lens at the nanometer length-scale. The optical lens is essentially a means to perform *Fourier* transforms (FFTs) to real time optical signals and hence the merits of realizing a lens at this scale is directly tied to the importance of *Fourier* transform in performing various computational and signal processing tasks. The lens design presented here achieves desired material parameters by means of manipulating the geometric configuration of subwavelength inclusions made from two materials, i.e., silver and a moderate dielectric material. A 2D equivalent of this concept has already been introduced in [20] but a 3D version had not been examined due to the lack of efficient computational tools that made

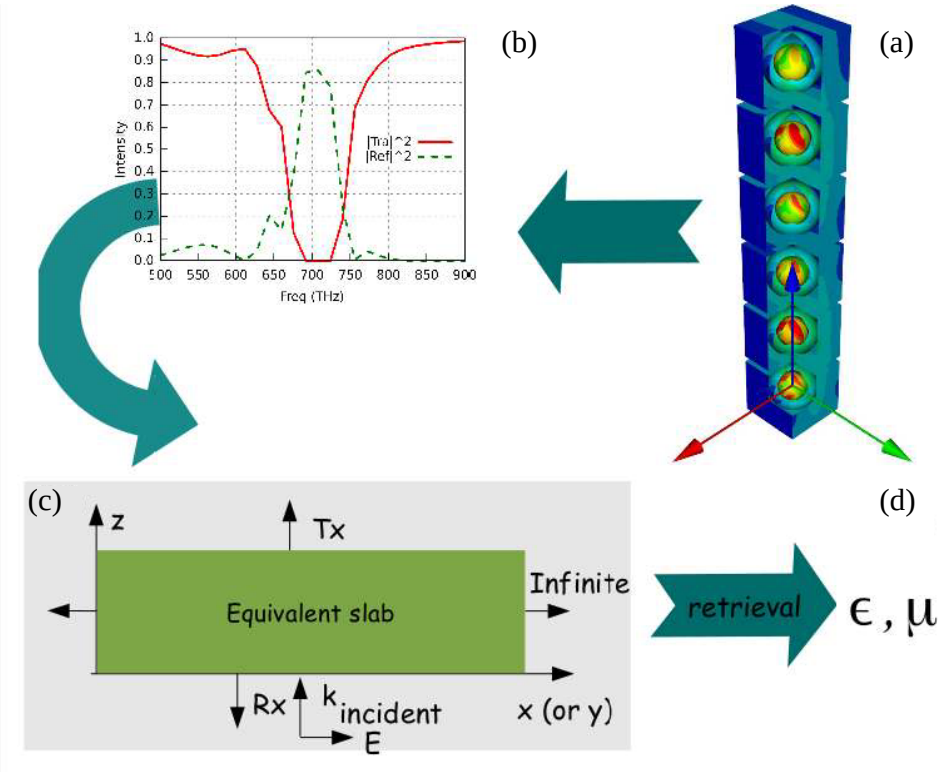

Figure 3. The process for numerical retrieval of equivalent material properties using (a) a numerical solver capable of solving doubly periodic infinite problems, (b) extraction of reflection and transmission data over a frequency range, (c) matching the reflection and transmission data to that of an analytical infinite slab model and finally obtaining the equivalent constitutive parameters as obtained in (d).

such numerical analysis nearly impossibly to archive. Using the A-IE-FFT solver, however, a full-wave analysis of the complete structure can be carried out, allowing for detailed examination of potential design challenges and bottlenecks. The 3D digital MM building blocks used in this design are made from two possible configurations of spherical core-shells, i.e., silver-coated dielectric cores and and dielectric-coated silver cores.

4.1.1. Bulk Properties

Bulk material properties for core-shell arrays can be obtained via analytical methods provided that building block dimensions are sufficiently smaller than the operation wavelength. In this design, however, a lattice periodicity of $d_x = d_y = d_z = 92\,\text{nm}$ is used which at the operating frequency of $f = 640\,\text{THz}$ measures $\frac{1}{5}\lambda_0$, $\lambda_0 = 468\,\text{nm}$ being the free space wavelength. Hence, the constitutive material parameters of the equivalent bulk matter shall be obtained by means of numerical retrieval, i.e., matching the transmission and reflection of infinite periodic arrays of the individual building blocks to that of an infinite slab with the same thickness to seek out constitutive material parameters. Here, as depicted in Fig. 3, the transmission and reflection for a periodic configuration of a 6 layer periodic array

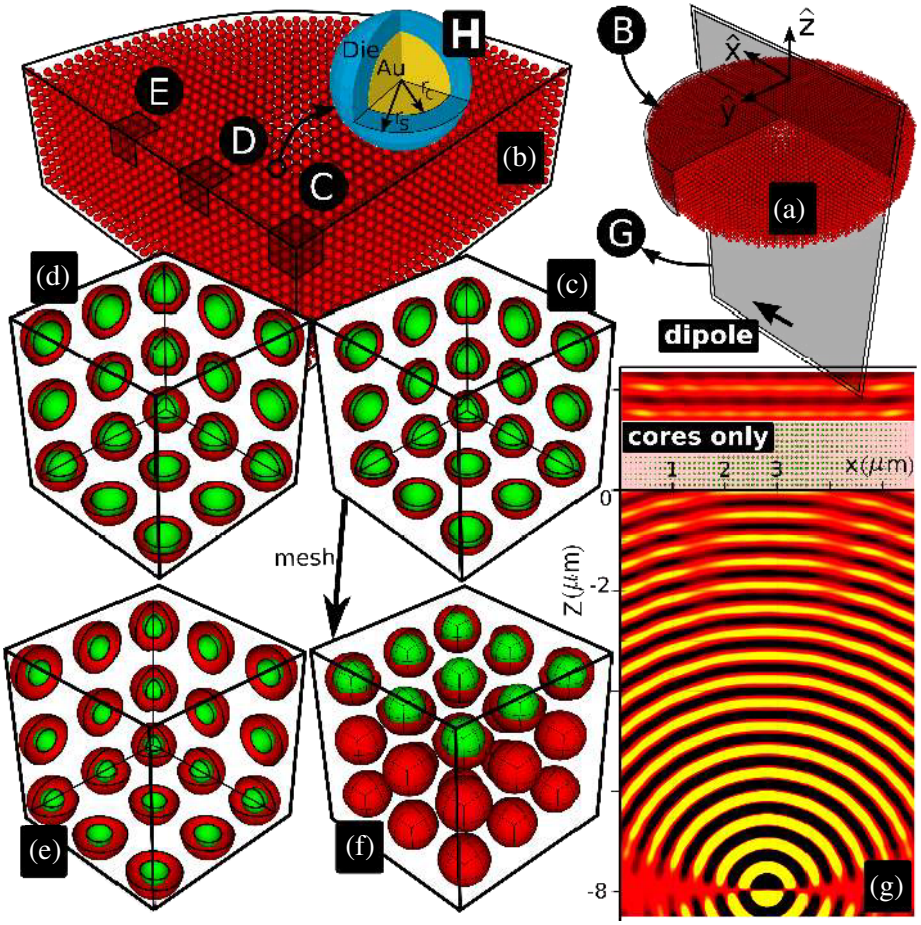

Figure 4. Digital lens, 346.6 million unknowns. (a) The complete core-shell lens excited with a dipole source on the axis of the lens, (b) a quarter of the lens enlarged, (c)–(e) as depicted in B, these are small segments of the lens cut open to reveal the core-shell construction. The green surfaces are the outside boundary to metal region and the red surface are the outside boundary to the dielectric region. (f) A different cut of E also depicting the high-order curvilinear mesh, a key to reducing computational cost (g) real part of the y-component of magnetic field in a constant x plane a indicated in A, (h) general construction of a core-shell building block.

Table 1. Numerically retrieved material properties for various core-shell configurations at $f = 640\,\text{THz}$. Note that negative imaginary parts imply losses due to the choice of $e^{\jmath\omega t}$ ansatz. r_c signifies core radius.

r_c	Core	Shell	$\Re\epsilon_r$	$\Im\epsilon_r$	$\Re\mu_r$	$\Im\mu_r$
31.99	Die	Ag	1.17	−4.7E-3	0.978	3.4E-3
30.44	Die	Ag	1.06	−3.0E-3	0.982	3.7E-3
29.35	Die	Ag	0.96	−1.6E-3	0.988	4.7E-3
28.54	Die	Ag	0.86	3.5E-3	0.991	5.8E-3
13.83	Die	Ag	2.66	−0.1172	0.283	1.8E-2
12.72	Die	Ag	1.62	−0.2593	0.420	7.5E-2
27.27	Die	Ag	0.66	1.2E-2	0.970	−7.3E-3
4.910	Die	Ag	3.42	1.5E-2	0.752	9.6E-4
26.61	Ag	Die	3.08	3.7E-2	0.782	−1.9E-3
23.40	Ag	Die	2.78	4.2E-2	0.806	−3.1E-3
21.11	Ag	Die	2.51	4.1E-2	0.829	−3.6E-3
19.31	Ag	Die	2.28	3.7E-2	0.849	−3.9E-3
17.76	Ag	Die	2.09	3.3E-2	0.866	−4.5E-3
16.28	Ag	Die	1.94	3.1E-2	0.874	−5.7E-3
14.76	Ag	Die	1.67	−4.4E-2	0.944	3.2E-2
13.04	Ag	Die	1.56	2.1E-2	0.939	4.3E-3
10.90	Ag	Die	1.42	7.8E-4	0.953	2.7E-3
7.56	Ag	Die	1.28	−3.4E-3	0.969	2.9E-3

of core-shells with the fixed lattice size of 92 nm are obtained via full-wave simulation. For simplicity, it is assumed that all building blocks are made of core-shells that share the same external radius of 33 nm while the core radius is varied as a control parameter to achieve the desired properties. Table 1 lists the achievable constitutive parameters by means of varying the core dimensions for two different material configurations, one with silver-coated dielectric spheres and the other with dielectric-coated silver spheres. For these models, the relative permittivity of silver and silica, $\epsilon_{r,\text{Ag}} = -6.55 - \jmath 0.08$ and $\epsilon_{r,\text{SiO}_2} = 2.24$ were obtained from [21] and [22].

4.1.2. A 12-Layer Lens Design

This lens is realized using a 12 layer construction of core-shells with the same fixed lattice size of 92 nm used in the retrieval process as mentioned in the previous section. The phase profile of the lens follows $\Delta\phi = \frac{2\pi}{\lambda_0}(\sqrt{\rho^2 + F^2} - F)$ where F and ρ, respectively denote the focal distance of the lens and the radial distance from the center of the lens. All of the core-shells used in this design are made from dielectric coated silver cores. Fig. 4, depicts the details of the geometrical design of the lens. At $\lambda_0 = 468\,\text{nm}$, the lens is designed to have a full phase cycle with the focal distance of $F = 17\lambda_0$ and thus the lens measures 61 building blocks in diameter and consists of 45136 core-shell particles. The computer model used for this problem is constructed from 36 different types of building blocks to cover the 360° phase cycle with a resolution of 10°. Depicted in Fig. 4(g), is the real part of the electrical field induced by an $\hat{x}$-oriented dipole source located at the focal point of the lens in the lower $z < 0$ half space. Fig. 4(g) compares the induced field in presence and absence of the lens. As expected from the design, the digital MM lens transforms the curved wavefront of the dipole source into a flat wavefront and this can be confirmed by looking at the phase distributions at the input and output planes of the lens as it is shown in Fig. 5. The numerical simulation in this section uses a set of 36 building blocks each consisting of three core-shells arranged in a $61 \times 61 \times 4$ lattice filled with 11284 cells (33852 core-shells). The final linear problem involves solution of a linear system with $34,664,448$ ES unknowns or total of $93,184,896$ surface unknowns.

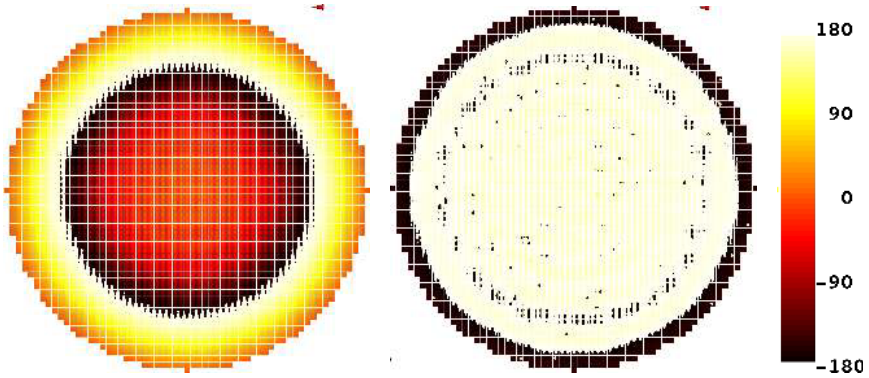

Figure 5. Plot showing the phase of total E_x on the two planes right before and after the the 12 layer lens. The tiny red arrow on the top signifies $\hat{x}$ direction.

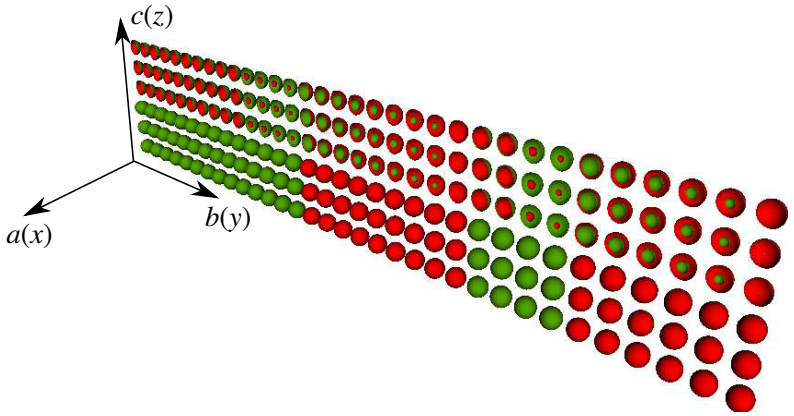

Figure 6. Core-shell construction of a thin slice of the 6 layer lens starting from the center of the lens (left) all the way to the outside edge. The green surfaces signify the exterior boundary of dielectric and green surface signify the exterior boundary of silver. The upper three layers have been sliced through to reveal the interior details. The a, b and c axes are parallel to $\hat{x}$, $\hat{y}$ and $\hat{z}$ unit vectors. The figure shows the evolution of building blocks starting from the center of the lens (on the left) all the way to the outmost radius (on the right). See how the lens begins (at the center) with dielectric-coated silver spheres and ends with silver-coated dielectric spheres.

4.1.3. A 6-layer Lens Design

The amount of phase variation one can achieve across a flat lens is a direct function of the range of effective refractive index and the thickness of the lens. In an attempt to reduce the thickness of the flat lens, one can extend the variety of building blocks by including silver-coated dielectric cores as it can be seen from the thin slice shown view in Fig. 6. As evident from Table 1, this can extend the range of achievable constitutive parameters and hence allow for achieving a complete 360° phase cycle while reducing the thickness of the lens from 12 to 6 layers. The lens design attempted here consists of 6 layers of core-shells and measures 65 building blocks in diameter. Moreover, to examine how rapidly the material properties can be varied before violating the local periodicity condition, a shorter focal distance of $F = 9\lambda_0$ is used for the design. The shorter focal distance results in a *Fresnel* type lens in which more than one 360° phase cycles are covered. It is worthwhile mentioning that the shorter focal distance results in more rapid phase variation particularly as we depart from the central portion of the lens. Using the A-IE-FFT solver, a full wave simulation is adopted in which the lens is excited with an $\hat{x}$-oriented dipole source at the focal point in the lower $z < 0$ half space. Fig. 7, depicts the phase distribution on the two planes right before and after the lens. By looking at the phase distribution on

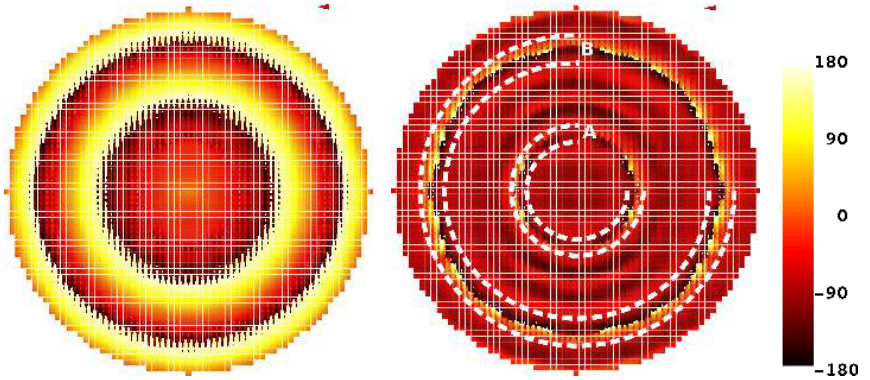

(a) $z = 0$ nm (b) $z = 12{\times}2$ nm (c) legend

Figure 7. Plot showing the phase of total E_x on the bottom and top planes of the 6 layer lens. On the bottom, the input phase due to the dipole covers two complete 360° phase cycles as expected from the location of the dipole with respect to the lens. On the top plane, i.e., the output of the lens, the lens has failed to produce the expected constant phase. The tiny red arrow on the top signifies $\hat{x}$ direction.

the top plane of the lens, it is evident that the desired phase transformation has not been achieved. This can be attributed to the rapid variation of building blocks which in turn violates the local periodicity assumption. Referring to Fig. 7, two circular regions of undesired phase fluctuation are depicted by white dashed lines (labeled as A and B). Strong undesired phase deviations occur in these two regions that correspond to a rapid change in the core radius of the core-shell building blocks. Closer examination reveals that A, corresponds to a change of core radius from 28 nm to 14 nm as one moves towards the outer radius of the lens. Similarly in B, a core radius variation from 13 nm to 9 nm has occurred. One possible remedy to this problem is, of course, to reduce the building block dimensions which is, among other things, subject to limitations in nanometer scale fabrication. Nevertheless, using the A-IE-FFT method, the designs can be easily examined and studied prior to investment in the fabrication of the device.

4.2. Beam Tilting Metasurface

Metasurfaces are receiving widespread attention due to their ease of fabrication in planar structures that lend themselves to existing fabrication tools and techniques. As a general guideline, metasurfaces are designed to control or transform phase and/or amplitude of waves as the waves travel through a sheet of finite thickness that often measures considerably smaller than the incident wavelength. The finite thickness factor, is another practical merit in metasurface design that makes them amenable to stacking allowing for realization of complex transformational optics systems.

4.2.1. Building Blocks

The metasurface presented in this section is operated at 200 THz and consists of building blocks that are arranged in a square lattice with lattice constant $d_x = d_y = 400$ nm (see Figs. 8(a)–(d)). The entire structure is assumed to live in a background medium with $\epsilon_r = 2.25$. As depicted in Figs. 8(g)–(h), building blocks of the metasurface are made from single or concentric double loop configurations of silver lying in the xy. In the initial model, the rings are designed to exhibit a 20 nm thickness along the z direction. The inner and outer diameter of the loops are used as control parameters to achieve desired phase and amplitude response. Hence, four control parameters (D_1, D_2, D_3, D_4) are given per building blocks consisting of two concentric loops and two control parameters (D_1, D_2, 0, 0) are given for building blocks consisting of a single loop. Since the individual building blocks measure much shorter than the wavelength along the propagation direction of the incident field $\hat{z}$, they can be treated as lumped elements with given admittance that can be controlled via the control parameters. The correspondence between the control parameters and the effective admittances is obtained by means

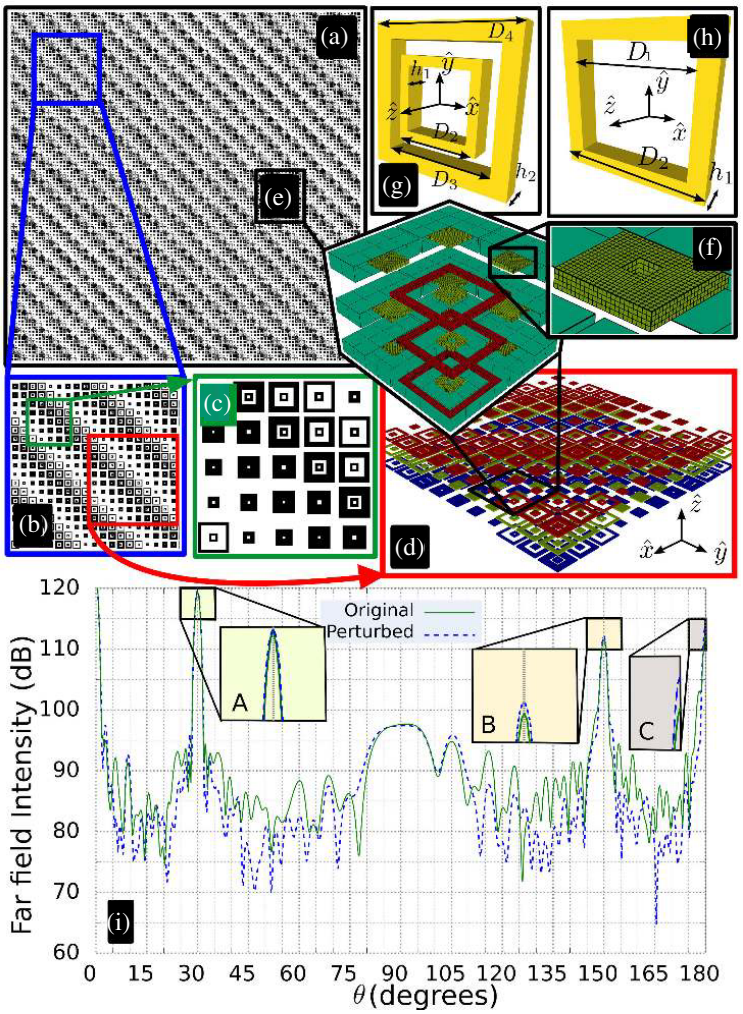

Figure 8. Beam tilter, 462–518 million unknowns (a) Shadow view of the top layer of the three layer structure of the beam-tilter, (b)–(c) zooming into smaller portions of the top layer, (d) the 3D view corresponding to a smaller fraction of B (use of color only to enhance visibility), (e) zooming into a smaller fraction of D while displaying the mesh on the rings and the ES, (f) further zooming into an even smaller fraction of E to reveal the mesh on one of the building blocks, (g)–(h) basic concentric and single ring building blocks, (i) far field intensity of the scattered field in the $\phi = 225°$ plane.

of numerical simulation of infinite periodic configurations of the individual loops. Hence, once again, the assumption of local periodicity, which may be violated when the building blocks are integrated into the final array, is key to the design procedure of the beam tilter. An initial examination of the plasmonic rings using an infinite periodic lattice, indicates that a limited range of transmission phase can be achieved using the single and double ring topologies [23, 24] depicted in Fig. 8(g) and Fig. 8(h). Therefore, as shown in Fig. 8(D), a three-layer cascaded combination is used to realize a complete 360° span of phase transmission while maintaining minimal return losses and high transmission intensities [25–27]. Since a single layer of such loop array is not sufficient to provide the desired transmission phase while maintaining a high level of transmission. Thus, three cascading layers of loop configurations with a dielectric spacer medium and a spacing of $\lambda/4$ are used to achieve the desired transmission phase and amplitude characteristics. The equivalent circuit model of one effective building block is shown in Fig. 9. The equivalent circuit model is used to calculate the resulting transmission phase and amplitude for a the given equivalent admittances of Y_1, Y_2 and $Y_3 = Y_1$ that can be controlled via changing the geometric parameters of the individual (single/double) loop building blocks [25, 26].

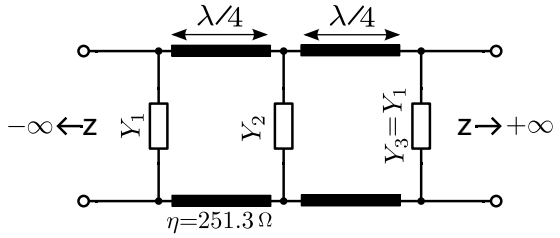

Figure 9. Equivalent circuit model for the three layer combination of $\frac{\lambda}{4}$-separated building blocks.

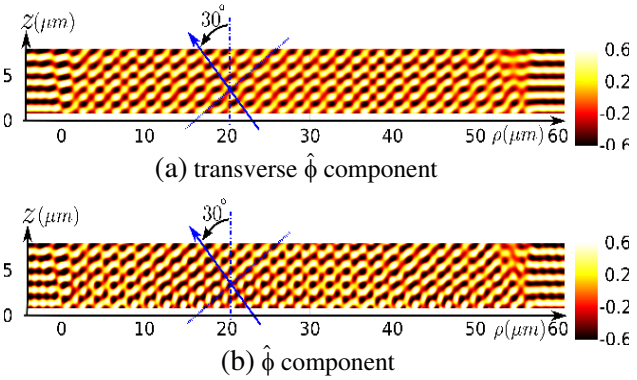

Figure 10. Total electrical field above the beam tilter on $\phi = 225°$ plane. The lens sits in a $-0.2\,\mu\text{m} < x < 40.2\,\mu\text{m}$, $-0.2\,\mu\text{m} < y < 40.2$ region. Therefore, on the $\phi = 225°$ plane, the region $-0.282\,\mu\text{m} < \rho < 56.85\,\mu\text{m}$ is right above the lens. Therefore, some unperturbed plane wave propagating along $\hat{z}$ can be observed on the left and right tails of the image.

4.2.2. Array Design

Denoting the intended beam direction by means of spherical coordinates $\theta = \theta_t = 30°$ and $\phi = \phi_t = 225°$ and assuming λ is the propagation wavelength in the background medium, the intended beam must exhibit a phase profile of $\gamma = \frac{2\pi}{\lambda}(\sin(\theta_t)*\cos(\phi_t)+\sin(\theta_t)*\sin(\phi_t))\cdot(x, y)$ when observed on a $z =$ constant plane. Thus, the intention is to have the building blocks, i.e., the three layer combination, that reproduce the aforementioned phase. Assuming the the local periodicity condition used in the design of the building blocks is not going to be severely violated, the building blocks are selected and placed in a finite $101 \times 101 \times 3$ array where a small portion of the array is visualized in Fig. 8. The A-IE-FFT solver is used to find the solution of the array in response to a plane incident field propagating along $\theta_{inc} = 0$ and $\phi_{inc} = 0$. Fig. 10 depicts the resulting total and scattered field. As it can be in Fig. 8, the peak at $(k_x, k_y) = k_0(\pm\sin(\theta_t)\cos(\phi_t), \pm\sin(\theta_t)\sin(\phi_t))$ which is 8 dB above the other three bragg modes, corresponds to the intended beam. The half power beam width along θ is as small as 1.5° as the array measures $40 \times 40 \times \frac{1}{2}\lambda^2$ where λ is the propagating wavelength in the background medium. The final simulation uses a set of 48 building blocks arranged in $101 \times 101 \times 3 = 30603$ cells. The final linear problem involves solution of a linear system with $94,012,416$ ES unknowns or total of $462,459,664$ surface unknowns.

4.2.3. Modeling Random Defects

The satisfactory results of Fig. 8 suggest that the proposed design can be a good candidate for actual fabrication. However, regardless of the techniques used for fabrication, accurate fabrication of large scale is prone to a variety of inaccuracies and defects the nature of which is highly tied to the actual method of fabrication. Therefore, proper yield analysis is key to the actual verification of the design if it is intended for real world fabrication. Without getting into fabrication specific details, here we perturbed the initial design of the beam tilter as listed below. In the following, three important building block design parameters, i.e., h or the thickness of the metal rings along $\hat{z}$, $a = D_1$ and $b = D_2$ in single ring building blocks and $a = D_1$ and $b = D_3$ for double ring building blocks are perturbed while the building blocks are deterministically and randomly displaced in the xy plane to account for fabrication inaccuracy and inter-layer registration issues. Note that the sequence of the following perturbations follows the sequence of their actual imposition.

(i) To account for registration inaccuracy, the center of all building blocks in the bottom layer, i.e., layer 0, is shifted by $(\Delta x, \Delta y) = (-5\,\text{nm}, -5\,\text{nm})$, the center of all building blocks in layer 1 is

shifted by $(\Delta x, \Delta y) = (-5\,\text{nm}, +5\,\text{nm})$ to account for registration inaccuracy and the center of all building blocks in layer 2 is shifted by $(\Delta x, \Delta y) = (+5\,\text{nm}, +5\,\text{nm})$ to account for registration inaccuracy. The shifts on layers 0 and 2 are along the x-y components of $\vec{k}_t$ while the shift in layer 1 is orthogonal to the x-y component of $\vec{k}_t$, where $\vec{k}_t$ is the desired propagation vector for the tilted beam.

(ii) In all of the building blocks of all three layers, h is randomly perturbed by 5%.

(iii) The initial a and b dimensions of all of the building blocks in layer 1 and 2, are respectively scaled by a factor of 0.95 and 1.05 to reflect the fact that a separate process is used for their construction.

(iv) In all of the building blocks in layer 1 and 2, a and b are perturbed by 2.5%.

The far-field plot in Fig. 8, depicts the scattered far field intensity, i.e.,

$$10\log_{10}\left(\lim_{r\to\infty}\left(\frac{r}{e^{-\jmath kr}}\right)^2||E^{sca}||^2\right),$$

plotted in a set of $\phi =$ constant planes. Obviously the strongest peak occurs in $\phi = 225^\circ$ plane at $\theta = 30^\circ$ and the two peaks at $\theta = 0^\circ$ and $\theta = 180^\circ$ correspond to the forward and backward scattered field. The four peaks at $\theta = 30^\circ$ and $\theta = 150^\circ$ correspond $(k_x, k_y) = k_0(\pm\sin(\theta_t)\cos(\phi_t), \pm\sin(\theta_t)\sin(\phi_t))$. Obviously the peak at $(k_x, k_y) = k_0(\pm\sin(\theta_t)\cos(\phi_t), \pm\sin(\theta_t)\sin(\phi_t))$ corresponds to the intended tilt angle. Most importantly, this figure compares the far field response of the beam tilter under both the perfect and the above-mentioned randomly perturbed design, indicating that such perturbations are unlikely to have a major impact on the expected performance. From the view-point of computational expense, however, the modeling of the randomness was achieved with a moderate increase in the overall cost of the computation, since the randomness is directly translated to the presence of multiple, randomly perturbed, realizations for each building block. As a result of these perturbations, the final problem will use a set of 3×48 building blocks arranged in $101 \times 101 \times 3 = 30603$ cells. The final linear problem involves solution of a linear system with $94,012,416$ ES unknowns or total of $518,977,696$ surface unknowns.

5. COMPUTATIONAL STATISTICS

All numerical results presented in this work reflect highly challenging numerical problems that can be handled using the A-IE-FFT method. Making direct comparison with other computational methods and tools can be a difficult task. Thus, it is important to emphasize that the presented method is aimed at improving the computational modeling for a specific class of problems, namely array-based structures. In order to shed some light on the numerical complexity and the cost of solving these model problems we enlist some of the associated computational statistics. All problems were solved on a dual Xeon workstation with 16 physical CPU cores and the iterative solution process was terminated with a residual error in the order of 10^{-5}. Other detailed statistics can be found in Table 2 below. Note that Krylov Dim is a parameter associated with the iterative solver that determines the dimension of the iterative search space for the problem solution. The larger the Krylov Dim the better the convergence, however, this comes at the cost of requiring more memory.

Table 2. Comparison of some computational statistics.

Problem	ES Unknowns	cells	total unknowns	solve time	max memory	iterations	Krylov Dim
porous media	17,743,872	$19 \times 19 \times 8$	114,800,448	34	92 GB	190	30
12 layer lens	93,184,896	$12 \times 61 \times 61$	346,64,448	20	85 GB	120	20
beam tilt	58,757,760	$101 \times 101 \times 3$	462,459,664	170	138 GB	620	45
beam tilt (randomized)	94,012,416	$101 \times 101 \times 3$	518,013,552	219	125 GB	665	30

6. CONCLUSION

The A-IE-FFT is used for analysis and design of a family of optical MM structures for which the A-IE-FFT method is expected to deliver high computational efficiency. Exploiting this efficiency, we have been able to study and design complex MM systems. The concept of digital MM [20] design is thus, for the first time, applied to 3D structures. Also using the A-IE-FFT method, we have been able to conduct a basic study on the effects of random imperfections introduced in MM fabrication of a large and complex MM lens consisting of tens of thousands of building blocks.

ACKNOWLEDGMENT

This work is supported in part by the U.S. Office of Naval research (ONR) MURI award Grant No. N00014-10-1-0942 and in part by DARPA (via Grant No. N00014-14-1-0850).

REFERENCES

1. Strikwerda, J., *Finite Difference Schemes and Partial Differential Equations*, 2nd Edition, SIAM, 2004.
2. Taflove, A. and S. C. Hagness, *Computational Electrodynamics: The Finite-Difference Time-Domain Method*, 3rd Edition, 2005.
3. Solin, P., K. Segeth, and I. Dolezel, *Higher-order Finite Element Methods*, Chapman & Hall/CRC Press, 2003.
4. Strang, G. and G. Fix, *An Analysis of The Finite Element Method*, Prentice Hall, 1973.
5. Rao, S. M., D. Wilton, and A. W. Glisson, "Electromagnetic scattering by surfaces of arbitrary shape," *IEEE Trans. Antenna Prop.*, Vol. 30, No. 3, 1982.
6. Annigeri, B. S. and K. Tseng, "Boundary element methods in engineering," *Proceedings of the International Symposium on Boundary Element Methods: Advances in Solid and Fluid Mechanics*, 1989.
7. Lee, J., R. Lee, and A. Cangellaris, "Time-domain finite-element methods," *IEEE Trans. Antenna Prop.*, Vol. 45, No. 3, 1997.
8. Chew, W. C., "Computational electromagnetics: The physics of smooth versus oscillatory fields," *Phil. Trans. R. Soc. Lond. A*, No. 12, 2004.
9. Engheta, N., W. D. Murphy, V. Rokhlin, and M. S. Vassiliou, "The fast multipole method, FMM for electromagnetic scattering problems," *IEEE Trans. Antenna Prop.*, Vol. 40, No. 6, 1992.
10. Coifman, R., V. Rokhlin, and S. Wandzura, "The fast multipole method for the wave equation: A pedestrian prescription," *IEEE Ant. and Prop. Magazine*, Vol. 35, 1993.
11. Rokhlin, V., "Rapid solution of integral equations of scattering theory in two dimensions," *J. Computational Phys.*, Vol. 86, No. 2, 1990.
12. Song, J., C. C. Lu, and W. C. Chew, "Multilevel fast multipole algorithm for electromagnetic scattering by large complex objects," *IEEE Trans. Antenna Prop.*, Vol. 45, No. 10, 1997.
13. Phillips, J. R. and J. K. White, "A precorrected-FFT method for electrostatic analysis of complicated 3-D structures," *IEEE Trans. Computer-Aided Design Integration Circuits Syst.*, Vol. 16, No. 10, 1997.
14. Seo, S. M. and J. Lee, "A fast IE-FFT algorithm for solving PEC scattering problems," *IEEE Transactions on Magnetics*, Vol. 41, No. 5, 2005.
15. Barrowes, B., F. Teixeira, and J. Kong, "Fast algorithm for matrix-vector multiply of asymmetric multilevel block-toeplitz matrices," *Antennas and Propagation Society International Symposium*, 2001.
16. Li, M. and W. C. Chew, "Multiscale simulation of complex structures using equivalence principle algorithm with high-order field point sampling scheme," *IEEE Trans. Antenna Prop.*, Vol. 56, No. 8, 2008.

17. Li, M. and W. C. Chew, "Wave-field interaction with complex structures using equivalence principle algorithm," *IEEE Trans. Antenna Prop.*, Vol. 55, No. 1, 2007.
18. Burner, D., M. Junge, P. Rapp, M. Bebendorf, and L. Gau, "Comparison of the fast multipole method with hierarchical matrices for the Helmholtz-BEM," *CMES*, Vol. 58, No. 2, 2010.
19. Banjai, L. and W. Hackbusch, "Hierarchical matrix techniques for low and high frequency Helmholtz problems," *IMA Journal of Numer. Anal.*, Vol. 28, No. 4, 2008.
20. Della Giovampaola, C. and N. Engheta, "Digital Metamaterials," *Nat. Mater.*, Vol. 13, No. 12, 2014.
21. Johnson, P. and R. Christy, "Optical constants of the noble metals," *Phys. Rev. B*, Vol. 6, 1972.
22. Malitson, I. H., "Interspecimen comparison of the refractive index of fused silica," *JOSA*, Vol. 55, 1965.
23. Memarzadeh, B. and H. Mosallaei, "Array of planar plasmonic scatterers functioning as light concentrator," *Optics Letters*, Vol. 36, 2011.
24. Memarzadeh, B. and H. Mosallaei, "Multimaterial loops as the building block for a functional metasurface," *J. Opt. Soc. Am. B*, Vol. 30, No. 7, 2013.
25. Cheng, J. and H. Mosallaie, "Optical metasurfaces for beam scanning in space," *Optics Letters*, Vol. 39, No. 9, 2014.
26. Monticone, F., N. Mohammadi Estakhri, and A. Alù, "Full control of nanoscale optical transmission with a composite metascreen," *Physical Review Letters*, Vol. 110, No. 20, 2013.
27. Pfeiffer, C. and A. Grbic, "Cascaded metasurfaces for complete phase and polarization control," *Applied Physics Letters*, Vol. 102, No. 23, 2013.
28. Ansari-Oghol-Beig, D. and H. Mosalaei, "Array IE-FFT solver for simulation of supercells and aperiodic penetrable metamaterials," *Journal of Computational and Theoretical Nanoscience*, Vol. 12, No. 10, 2015.
29. Araujo, M. G., J. M. Taboada, J. Rivero, and F. Obelleiro, "Comprison of surface integral equations for left-handed materials," *Progress In Electromagnetics Research*, Vol. 118, 425–440, 2011.